Mitigating the ecological footprint of alkali-activated calcined clays by waste marble addition

Ludovico Mascarin [a], Hassan Ez-zaki [a], Enrico Garbin [a], Mark Bediako [b], Luca Valentini [a,*]

[a] *Department of Geosciences, University of Padua, via Gradenigo 6, Padua, Italy*
[b] *CSIR-Building and Road Research Institute, Kumasi, Ghana*

A R T I C L E   I N F O

A B S T R A C T

Low-CO_2, Portland-free cement binders can be produced by reaction of calcined clays in alkaline solutions, although the environmental footprint associated with alkaline activators may represent a point of concern. The amount of alkaline activator, and its embodied CO_2, can be reduced by partial replacement of calcined clay with waste marble. Fresh and hardened state properties, as well as compositional and microstructural evolution of alkali-activated blends of calcined clay and waste marble, were investigated by combining experimental methods with thermodynamic modelling. It was shown that substitution of calcined clay with 30% waste marble was beneficial to the workability and mechanical properties of alkali-activated binders and can mitigate drying shrinkage. The physical and chemical role of calcium carbonate and the composition of the reaction products were discussed, along with the role of carbonation reactions occurring by uptake of atmospheric CO_2. This approach can contribute to both reducing the CO_2 footprint of cement and upcycling potentially hazardous waste from the dimension stone industry.

1. Introduction

According to the latest Circularity Gap Report, over 90 Gt of resources were extracted from the Earth's crust in 2019 [1]. More than 40% of these resources fed the construction sector and it is estimated that a large share of this input is eventually emitted to the atmosphere as greenhouse gas, dissipated in the environment as unrecoverable waste or disposed of at facilities such as landfills and incinerators [1].

Finding a path towards a decarbonized construction industry is one of the issues to be addressed to mitigate greenhouse emissions associated with raw material sourcing and processing and, to this end, a great research effort is being committed to the design and production of building materials with reduced CO_2 footprint [2].

A transition to a greener construction industry also requires that a more sustainable supply chain is fostered by reducing the consumption of primary resources associated with cement and concrete production. One of the main concerns is represented by the consumption of sand and gravel resources, with a current demand that is exceeding the levels of sustainable sourcing [3]. Quarrying and excavation activities associated with the construction industry supply chain are also dramatically modifying the landscape with an impact comparable to that of geological agents [4].

Therefore, along with the need of deploying low-CO_2 binders, addressing the issue of raw material supply and disposal is mandatory if the construction industry aspires to a more circular approach in the near future.

In this paper, this topic was addressed by exploring the possible role of the stone industry waste as a secondary raw material in sustainable binders. It is estimated that about 200 Mt of quarrying and processing waste is produced out of a yearly gross dimension-stone production of 300 Mt [5]. Over 50% of the world stone production is represented by calcareous stone (limestone, marble) [5]. The generation of huge amounts of slurries during the cutting and polishing of marble poses a severe environmental issue in terms of disposal, since marble slurry and dust may contaminate soils and watercourses subsequent to mismanagement or heavy raining [6–8].

The use of waste marble in the construction industry can potentially mitigate the pressure exerted on disposal sites and facilities, and contribute to reducing the consumption of primary calcareous resources. Waste marble was used in OPC-based binary [9–12] and ternary [13] blends, as well as in alternative binders, including alkali-activated materials [14–16] and calcium sulfoaluminate-belite cement [17].

Here, we carried out a systematic study of the effect of replacing a fraction of calcined clay with 30 wt% to 50 wt% waste marble, in

Table 1
XRF composition (wt.%) of waste marble (top) and clay soil (bottom)

SiO$_2$	TiO$_2$	eAl$_2$O$_3$	Fe$_2$O$_3$	CaO	MgO	Na$_2$O	K$_2$O	LOI
0	0	0.1	0	55.9	0.6	0	0	43.4
64.7	0.1	25.8	1.0	0.1	0	1.3	0.7	6.3

Table 2
Mix design (quantity in grams) and resulting elemental ratios, w/c and Na$_2$O$_{eq}$. Elemental ratios were computed by XRF composition and mix design.

Mix	Clay source	Waste marble	Alkaline solution	Extra water	Na/Al	Si/Al	Ca/Al	H/Na	w/c	Na$_2$O$_{eq}$
WM0	50	0	40.2	5.7	0.85	2.75	0	14.39	0.45	11.0
WM30	35	15	28.3	8.4	0.85	2.75	0.80	17.43	0.41	8.4
WM40	30	20	24.2	9.7	0.85	2.75	1.24	19.46	0.40	7.4
WM50	25	25	20.1	11.0	0.85	2.75	1.86	22.31	0.39	6.3

alkali-activated binders, which may represent a potential sustainable alternative to Portland cement [18].

Previous studies investigated the effect of calcium carbonate additions on the properties of alkali-activated binders based on metakaolin [19–21] or calcined halloysite [22]. In these studies, the amount of alkaline activator was kept constant, independent of the amount of aluminosilicate material substituted with calcium carbonate. More recent studies implemented a different approach in which the amount of alkaline activator was reduced proportionally to the quantity of calcium carbonate added, such that the bulk Na/Al ratio of the binder remained constant [23–25]. In this way, the addition of calcium carbonate has the further benefit of reducing the ecological footprint (and cost) of the alkaline activator, which is the main contributor to CO$_2$ emissions in alkali-activated materials [26,27], considering that the global warming potential of sodium silicate is about 1 kg CO$_{2eq}$ per kg produced [27]. In the present study, we followed this latter approach, but compared to the cited research: (a) waste marble was used in place of limestone; (b) nearly pure, commercial metakaolin was replaced with a locally sourced, low-grade clay soil, which represents a less expensive alternative; (c) the effect of CaCO$_3$ substitution on additional properties other than compressive strength, such as workability and dimensional stability, was investigated in detail. Moreover, the investigated properties were discussed in relation to the mineralogical and microchemical composition of the reacted binders, assessed by means XRD, spot SEM-EDS analysis and thermodynamic modelling.

2. Materials and methods

2.1. Raw material characterization

Waste marble slurry was obtained from the Carrara quarries, where 3 Mm^3 of waste deriving from cutting, polishing and processing are produced each year [28]. A fine powder (d_{50} = 12.5 μm by laser particle size analyser) consisting of calcite, with minor dolomite impurities, was obtained after oven drying at 60 °C for 24 h and subsequent grinding. The clay soil was sampled in the Atwima Nwabiagya district (Ashanti region, Ghana). The collected soil was sieved according to EN 933-1 [29] and the fraction with d_{50} = 9.4 μm was used for the analyses. Differential particle size distributions of the used raw materials are displayed in Fig. 1 (left).

The XRF chemical composition of the raw materials is reported in Table 1. The XRD composition of the clay soil was obtained with an X'Pert Pro diffractometer (Malvern-Panalytical) equipped with a Co-anode X-ray source (40 kV, 40 mA) and an X'Celerator detector. The clay was micronized and blended with 10 wt% ZnO standard before running the measurement. Rietveld quantitative phase analysis was performed using the Profex/BGMN software [30]. The results of the quantitative phase analysis indicated that the raw material mainly consisted of quartz (48.3 wt%) and kaolinite (39.9 wt%), with minor amounts of paragonite (7.1 wt%) and illite (4.7 wt%).

Prior to alkali activation, the clay soil was calcined in a laboratory muffle at a temperature of 800 °C for 5 h, with a heating rate of 10 °C min^{-1}. This combination proved to be the one that, in a preliminary experimental design study, allowed engineering properties to be optimized [31]. Heat flow and weight changes were simultaneously measured on 2 g of powder placed in a crucible, from room temperature to 1200 °C with a built-in air flow and heating rate of 10 °C min^{-1}.

The DTG-DSC curves are displayed in Fig. 1 (right). DSC results suggested the loss of adsorbed and interlayer water between 100 and 300 °C. The main temperature interval of kaolinite dehydroxylation was in the range 400–700 °C, in agreement with the published literature [32–35]. The change in the slope of the DTG curve occurring around 550 °C was possibly due to the onset of paragonite decomposition. In the DSC curve, this transition overlapped with the solid–solid transition from α-quartz to β-quartz, occurring at 573 °C [36]. A single-crystal study on 2M$_1$-paragonite and its dehydroxylated phase revealed a clear increase in the rate of cell volume expansion between 600 and 700 °C [37]. Above this temperature, dehydroxylation of both paragonite and muscovite occur [38]. The wide exothermic peak centred around 900 °C visible in the DSC curve was associated with feldspar formation [39]. The second peak, close to 1000 °C was ascribed to the crystallization of a pseudo-mullite with γ-Al$_2$O$_3$-type structure resulting from metakaolinite decomposition [40]. Based on these results, the selected temperature of clay calcination (800 °C) allows complete dehydroxylation and amorphization of kaolinite, meanwhile preventing crystallization of inert phases.

The XRD pattern of the clay soil prior and after the thermal treatment is displayed in Fig. 2. Illite (10 Å) and paragonite (9.7 Å) have peaks at low-angle, followed by the main peak of kaolinite at ~14° 2θ (7 Å). Complete structural breakdown of kaolinite and paragonite, subsequent to calcination, were deduced from the disappearance of the associated peaks. The peaks of illite, or partially dehydroxylated illite, persisted after calcination. Peaks associated with feldspar were detected by XRD after calcination, indicating that incipient feldspar crystallization began at a lower temperature compared to what suggested by the results of thermal analysis.

The specific surface area of the calcined clay soil (3.8 m^2/g) was measured on a Micromeritics ASAP 2020 Plus instrument, using nitrogen absorption and the Brunauer–Emmet–Teller (BET) method.

2.2. Mix design and procedure

The calcined clay was blended with different amounts of waste marble powder (0 wt%, 30 wt%, 40 wt%, 50 wt%).

An alkaline solution with SiO$_2$/Na$_2$O molar ratio equal to 1.6 and concentration equal to 40.5% was prepared by mixing 1000 g of a reagent grade sodium silicate solution (SiO$_2$/Na$_2$O molar ratio equal to 2.6 and concentration equal to 37.5%) with 86 g of NaOH flakes, with low intensity stirring, 24 h prior to the preparation of alkali-activated pastes. The selected value of SiO$_2$/Na$_2$O molar ratio was based on preliminary experiments by which it was observed that efflorescence tend to develop for lower values, and limited setting, with development of surface cracks, occurred for higher values.

Small batches of 50 g of powder (calcined clay + waste marble) were activated with the above sodium silicate solution and an additional amount of water to provide optimal workability. A vertical stirrer was used to mix the alkali-activated pastes (1 min at 250 rpm + 2 min at 400 rpm).

The mix design, performed with the aid of the AMiDsT software [41], and corresponding elemental ratios are reported in Table 2. The Na/Al ratio was kept constant at 0.85, to avoid any possible efflorescence, which is likely to occur when this ratio is higher than 1 [42], due to an unbalance between the amount of sodium in solution and the amount of reactive alumina. To keep this ratio constant,
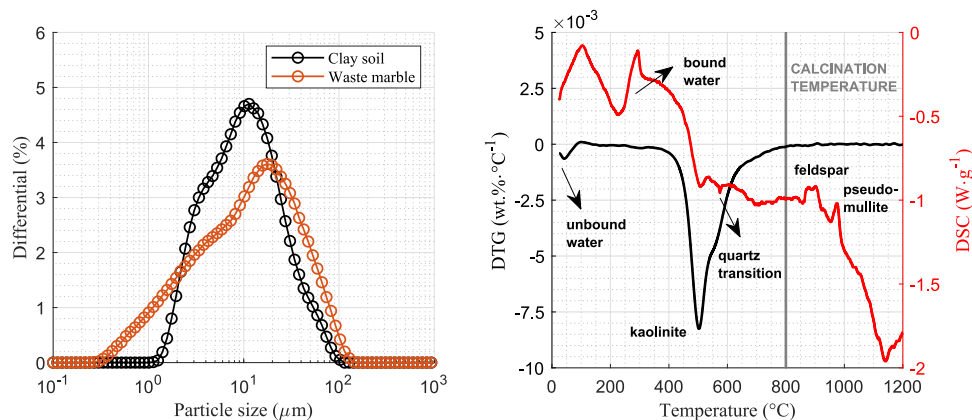
Fig. 1. Particle size distribution of the clay soil and waste marble (left) measured with a Bettersizer SD (Dry) analyser; Derivative thermogravimetry DTG curve and differential scanning calorimetry DSC curve (right) measured with a Mettler Toledo TGA/DSC 3+.
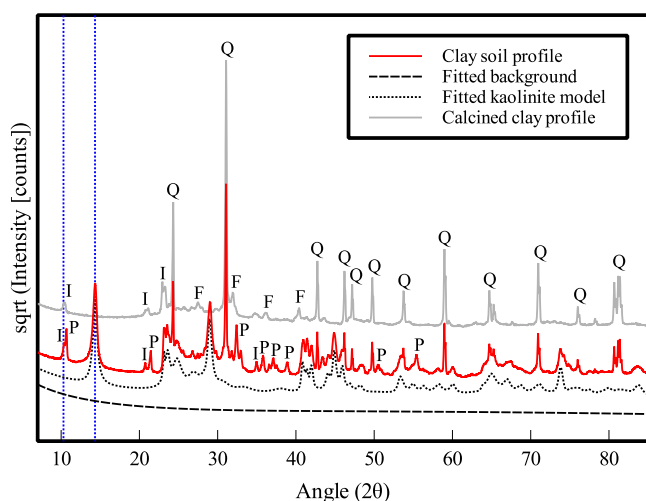

Fig. 2. XRD pattern of the raw clay. Continuous red line: raw clay observed pattern; black dotted line: fitted kaolinite model; black dashed line: fitted background; continuous grey line: calcined clay observed pattern. Phase labels: I (illite); P (paragonite); Q (quartz). The blue dotted lines highlight the position of the low-angle peaks of illite and kaolinite. (For interpretation of the references to colour in this figure legend, the reader is referred to the web version of this article.)

it was necessary to reduce the amount of alkaline activator used, proportionally to the fraction of waste marble added. Table 2 also displays the value of equivalent Na_2O, which is proportional to the amount of alkaline activator in the mix, hence providing a quantitative descriptor of associated global warming potential. The total amount of water, consisting of the mass of solvent in the activator plus any deionized water added to the mix, was expressed as the mass of total water divided by the total anhydrous mass in the mix (calcined clay + waste marble + sodium and silicon oxides present in the activator). This expression corresponds to the standard water-to-cement ratio for a Portland cement, hence the abbreviation w/c used. The total amount of water was slightly decreased proportionally to the amount of waste marble in order to maintain a constant flow diameter of 55 mm, measured by means of a mini-slump test using 7.8 cm³ of fresh paste, which allowed optimal mixing, with no bleeding, to be achieved.

2.3. Early-age properties

The viscosity of the alkali-activated pastes was investigated by means of a stress-controlled rheometer Anton Paar MCR92 with plate-plate geometry (lower plate diameter = 50 mm, upper plate diameter = 25 mm). The gap was set at 2 mm and the temperature held constant at 20 °C. A solvent trap was used to prevent evaporation during the measurement. Flow curves were measured on pastes mixed for three minutes, using a triangular procedure in logarithmic ramps of shear rate of 10^{-4} s^{-1} to 10^2 s^{-1} allowing 2.5 s measuring time per point. The measurements were preceded by a pre-shear of 1 min at high oscillation amplitude of 10% and a constant frequency of 10 Hz. Structure recovery was performed at low oscillation of 5×10^{-3} % and frequency of 1 Hz for 2 min. All presented data were obtained from the analysis of the ramp down measurements.

The viscoelastic properties were investigated by means of amplitude oscillatory shear strain tests, by which the storage (elastic component) and loss (viscous component) moduli were determined. During the oscillatory tests, the shear strain was increased from 10^{-2}% to 10% in logarithmic ramps, maintaining a constant frequency of 1 Hz and a temperature of 20 °C.

Early-age shrinkage was measured on fresh pastes using a time-lapse X-ray imaging approach. The alkali-activated pastes were poured in cylindrical plastic holders (3 cm height and 1.4 cm diameter) and placed in the X-ray chamber immediately after mixing. The temperature inside the specimen chamber was 29 ± 1 °C and the ambient relative humidity 55 ± 3%. X-ray attenuation images with 3.45 μm pixel size were collected each 15 min, over an interval of three hours. The final dataset consisted of a time sequence of 12 digital images for each sample, displaying the time-dependent vertical interface displacement resulting from capillary stresses and particle settling. These digital images were used to calculate the early strain. A detailed explanation of this method can be found elsewhere [43].

2.4. Hardened-state properties

Volume stability was assessed by measuring the strain of samples by means of digital length comparators having an accuracy of 2.5 μm. This approach was used for the measurement of shrinkage in alkali-activated materials [44–46]. The alkali-activated pastes were kept in cylindrical plastic holders (same size as above) at 95% RH and ambient temperature. After two days, the hardened pastes were removed from the plastic holders and the reference length was measured. Then, the length variation was measured for seven days. The average RH during the measurement was 55%.

Compressive strength measurements were performed on prismatic samples, cast in teflon moulds of 6 × 1.5 × 1.5 cm³, after 7, 14 and 28 days (2 days curing at ambient temperature and 95% RH followed by curing at ambient conditions). These samples have the same aspect ratio of mortar prisms envisaged by the EN 196-1 standard [47]. The measurements were performed by placing the prisms horizontally between two metal platens having a 1.5 mm side, such that the load

was applied on a 1.5 × 1.5 cm^2 surface. Currently, no internationally recognized standard is available for testing the mechanical properties of alkali-activated materials, also because of the large compositional variability of such materials. Therefore, a hardened CEM I 52.5R cement paste with w/c = 0.5, sharing the same curing conditions and having the same size and shape, was tested at 7 and 28 days to serve as a reference.

The XRD mineralogical composition was measured on fragments from the compressive strength tests. These fragments were soaked in ethanol for 24 h to stop reaction [48,49] and subsequently dried at ambient temperature and micronized prior to the XRD measurement. The calcined clay was mixed with known quantities of waste marble (BB30 = 30 wt%, BB40 = 40 wt%, BB50 = 50 wt%), which consisted of 98.6 wt% calcite, and acted as an internal standard to quantify the amount of quartz in the calcined clay soil. The relative amount of quartz within the sample (BB0) was then normalized to the relative fraction within the alkali-activated mixes and used as an intrinsic standard with the aim of quantifying any change in the relative amount of calcite after reaction. We assumed that the reaction of quartz grains was negligible within the first 14 days of reaction. Furthermore, for validation, we measured the intensity ratio between the height of the [001] peak of quartz to the height of the [104] peak of calcite before and after reaction.

Microstructural and microchemical analyses were performed on polished sections of samples cured for 14 days, using a FEI Quanta 200 ESEM in BSE mode, operated at 20 kV with 4 μm spot size, equipped with an EDS detector. For each sample, the chemical composition of the matrix (i.e. the reaction product) was evaluated as the average at five different locations.

2.5. Thermodynamic modelling

Predicted phase assemblages were simulated using the GEMS model (http://gems.web.psi.ch) [50].

Thermodynamic data for metakaolinite were obtained from a previous modelling study [51]. A two-end-member N–A–S–H model, based on a thermochemical study of synthesized phases [52], was included in the database. This cited work reported the standard molar Gibbs free energy of formation of the two end-members. In the absence of data for the molar entropy of formation, we used the values for zeolite A [53] and zeolite Y [54], which were compositionally affine to the two N–A–S–H end-members. Crystalline zeolites were not considered in this study since they are normally kinetically hindered at ambient temperature, which is the curing condition relevant to the present study. The stoichiometry of the two end-members is: $(Na_2O)_{0.45}(Al_2O_3)_{0.45}(SiO_2)(H_2O)_{2.48}$ (N–A–S–H 1) and $(Na_2O)_{0.26}(Al_2O_3)_{0.24}(SiO_2)(H_2O)_{1.88}$ (N–A–S–H 2). The CNASH_ss solid solution model [55] was used for C–(N)–A–S–H. Na-based (trona: $Na_3(CO_3)$ $(HCO_3) \cdot 2H_2O$, thermonatrite: $Na_2CO_3 \cdot H_2O$) [56] and Ca–Na (gaylussite: $Na_2Ca(CO_3)_2 \cdot 5H_2O$, pirssonite: $Na_2Ca(CO_3)_2 \cdot 2H_2O$) [57] alkaline carbonates were also included in the database, with the aim of modelling the phase evolution in the presence of excess CO_2. These were the dominant alkaline carbonate phases that we observed by XRD in previous published [15] and unpublished studies on alkali-activated metakaolin. All other solid phases, as well as aqueous species, present in the simulations were based on the PSI-NAGRA thermodynamic database [58].

Simulating the interaction of the system with an external reservoir of CO_2 is not straightforward, as this represents an open thermodynamic system. Here, we used an approach similar to the one used in a GEMS-based thermodynamic modelling study of the carbonation of alkali-activated slag cements [59], in which the amount of CO_2 present in the system was progressively increased. A summary of all phases included in the database is reported in Table 3.

3. Results

3.1. Fresh properties

The behaviour of the alkali-activated pastes in response to the application of rotational shear is displayed in Fig. 3. In the low shear rate regime ($\dot{\gamma} < 1$ s^{-1}) the addition of waste marble enhanced the shear thinning behaviour, proportionally to its amount. The viscosity of the measured pastes was higher at very low shear rates in the presence of waste marble, with a crossover occurring near the shear rate value of 0.1 s^{-1}. Above this value and up to approximately 5 s^{-1} a reversal in the rheological behaviour was observed, with the measured viscosity decreasing proportionally to the amount of waste marble. At higher shear rates, the sample with no waste marble started to become significantly destructured and its viscosity fell rapidly. The results of the amplitude sweep tests are shown in Fig. 4. The values of the storage (G′) and loss (G″) moduli typically extend over a sub-linear region at small amplitude oscillation (linear viscoelastic region, LVE) then significantly drop at the critical strain value, where structural breakup occurs. Our samples showed similar values of the critical shear strain. The ratio of the storage to loss modulus in the linear viscoelastic region increased proportionally to the amount of waste marble present in the mix, indicating a progressively higher contribution of elastic forces as more calcined clay was substituted [61].

Early-age shrinkage strain was measured in two different configurations. The first set of samples was measured with the sample holders covered by a cap, which prevented evaporation of the aqueous solution. In this configuration (bleeding regime), the vertical displacement is mostly controlled by gravity-induced particle settling. The second set of samples was measured with the sample holders left uncovered, thus allowing evaporation (drying regime), which in turn leads to the development of capillary stresses [62], contributing to the overall shrinkage.

It was observed that, in the drying regime, the amount of strain increased nearly linearly during the first three hours, with the ultimate value varying between approximately 1% and 2%, proportionally to the amount of waste marble added to the mix (top part of Fig. 5).

In the bleeding regime, the formation of capillary stresses due to evaporation was prevented, and the overall strain was smaller for all samples (bottom part of Fig. 5). The ultimate strain varied between 0.1% and 0.4% for samples WM0, WM30 and WM40. For the sample with 50 wt% marble waste addition, the strain was significantly higher, with a value of more than 1% at 3 h, suggesting a strong tendency to particle settling. A previous investigation showed that the strain vs. time curves do not show discontinuities at measured setting times [63], implying that strain measured with this method is composed of both plastic shrinkage (due to particle settling, in the bleeding regime, and evaporation in the drying regime) and autogenous/drying shrinkage (bleeding/drying regime), considering the relatively short setting times of alkali-activated materials containing calcined clays [64–66]. These images also allowed the formation of bleed layers, and their time evolution, to be observed. In the sealed conditions (Fig. 6), no bleeding was observed for sample WM0, whereas a thin bleed layer developed for samples WM30 and WM40. The extent of this bleed layer was significantly larger for sample WM50, again indicating the stronger tendency to particle settling for this sample.

3.2. Hardened properties and microstructure

Contrary to what observed for early age shrinkage, the amount of strain measured for the hardened samples at later hydration stages decreased proportionally to the amount of waste marble added, with an observed reduction of up to 50% for sample WM50 (Fig. 7). For all samples, most of the observed strain occurred within the first day after the end of the curing period at higher RH. Similar abrupt volume variations were previously observed in alkali-activated materials [45,67].

Table 3
List of thermodynamic parameters of the solid phases used in the model.

|	ΔG_f^0 (kJ mol^{-1})	ΔH_f^0 (kJ mol^{-1})	S^0 (Jmol^{-1} K^{-1})	Ref
Metakaolinite	−3009.95	−3211.22	137.15	[51,60]
N–A–S–H end-members				
N–A–S–H 1	−2453.72	−2728.81	136.00	[52,53]
N–A–S–H 2	−1848.00	−2032.77	183.50	[52,54]
C–(N)–A–S–H end-members				
5CA	−2292.82	−2941.27	163.11	[55]
INFCA	−2342.90	−2551.26	154.50	[55]
5CNA	−2381.81	−2568.65	195.03	[55]
INFCNA	−2474.28	−2666.69	198.39	[55]
INFCN	−2452.46	−2641.96	185.58	[55]
T2C	−2465.40	−2720.71	167.00	[55]
T5C	−2516.90	−2780.27	159.90	[55]
TobH	−2560.00	−2831.43	152.80	[55]
Thermonatrite	−1288.53	−1432.00	168.10	[56]
Trona	−2381.12	−2682.10	303.13	[56]
Gaylussite	−3371.77	−3834.00	387.00	[57]
Pirssonite	−2658.27	−2956.00	239.00	[57]
Calcite	−1129.18	−1207.41	92.68	[58]
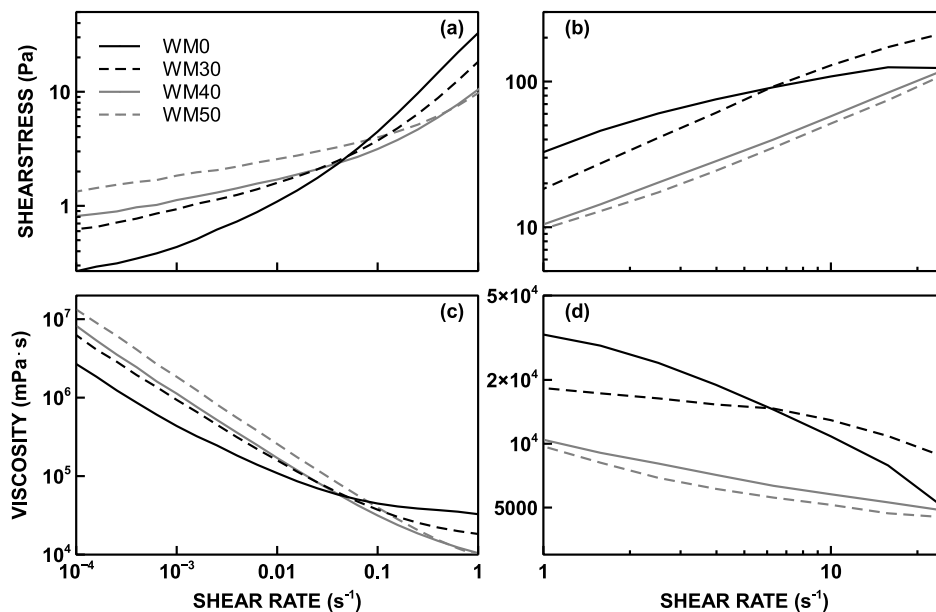
Fig. 3. Flow curves and viscosity curves for the alkali-activated pastes with different amounts of waste marble additions. The plots have been split in two shear rate intervals in order to facilitate reading. Flow curves for low shear rates ($\dot{\gamma} < 1$ s^{-1}) and high shear rates ($\dot{\gamma} > 1$ s^{-1}) are displayed in (a) and (b) respectively. Viscosity curves for the same shear rate intervals are displayed in (c) and (d).

Compressive strength development is summarized in Fig. 8. This figure also displays the value of Na$_2$O$_{eq}$ for each formulation, normalized to that of sample WM0. As previously explained, this parameter is used as a proxy of global warming potential, since it is proportional to the amount of alkaline activator, which in turn represents the most impacting factor in alkali-activated materials [26,27].

At 7 days, a maximum in the average compressive strength was observed for the sample with 30 wt% waste marble addition. The average compressive strength increased from 25.3 MPa (WM0) to 28.5 MPa (WM30), then dropped with further addition of waste marble, to values of 21.7 MPa (WM40) and 15.8 MPa (WM50). The 7-days compressive strength of the OPC sample, used as reference, was 34.3 MPa (55.9 MPa at 28 days). At 14 days, a similar trend was observed, with all samples increasing their strength by 50%–60% except the one with the highest waste marble addition, for which a small drop in compressive strength was observed. The maximum average compressive strength, observed for the sample with 30 wt% waste marble addition, was 42.0 MPa. Little or no increase in compressive strength was observed at 28 days. This was in agreement with previous observations showing that alkali-activated calcined clays develop most of their ultimate strength after 2 weeks [68]. A slight decrease was observed for sample WM40 and, to a larger extent (yet within the experimental error), for sample WM30, similarly to what observed in previous investigations of alkali-activated metakaolin–limestone blends [24].

Microstructural observation by SEM backscatter imaging revealed the presence, for sample WM0, of quartz grains and residual metakaolin, dispersed in a compact matrix (Fig. 9a, cracks formed upon sample preparation and polishing prior to SEM analysis). For samples with waste marble additions (Fig. 9b–d), it was observed that fine-grained calcite crystals acted as filler, being homogeneously dispersed within the matrix. The matrix appeared to be more porous proportionally to the amount of waste marble added to the mix.
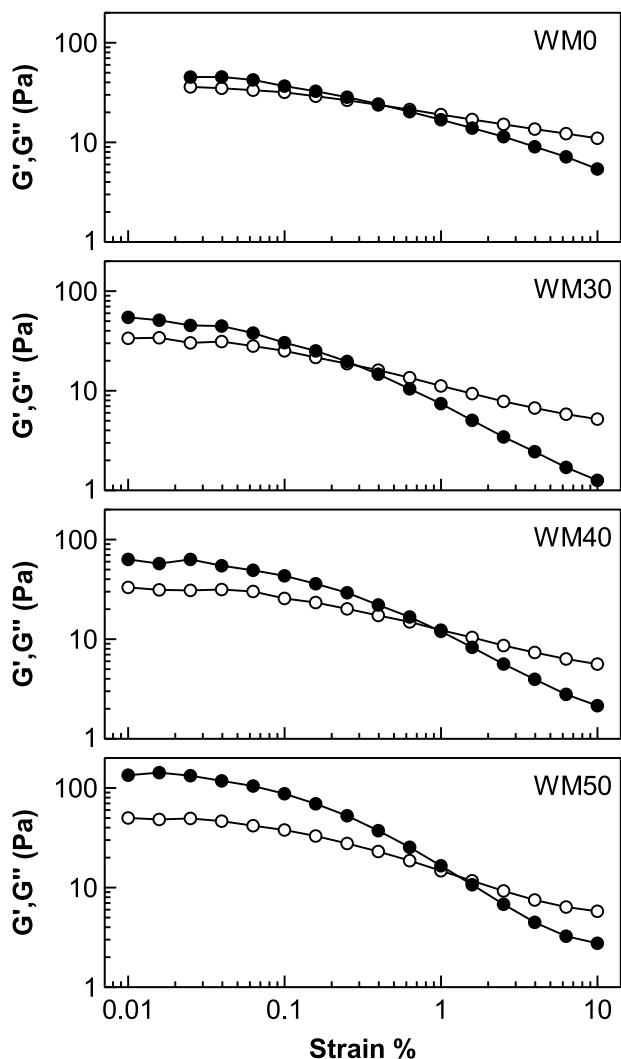
Fig. 4. Storage modulus (filled circle) and loss modulus (open circle) as a function of strain amplitude for the studied samples.
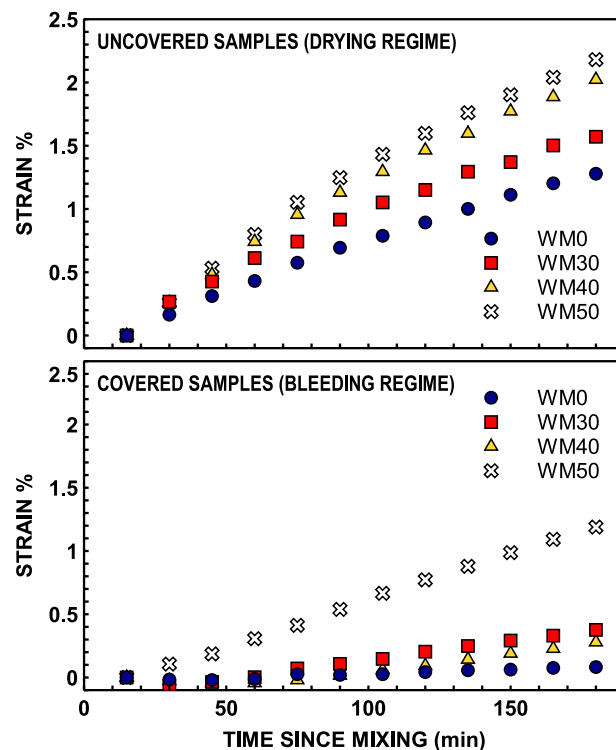

Fig. 5. Time variation of the early age strain, as measured by time-lapse X-ray imaging for the alkali-activated paste samples with different waste marble additions.

3.3. Mineralogical and microchemical composition

XRD patterns of the four blends prior to alkaline solution addition (BB0, BB30, BB40, BB50) are displayed with the patterns of the alkali-activated pastes after 14 days of reaction (WM0, WM30, WM40, WM50) in Fig. 10. The profiles were illustrated in a restricted 2θ interval to enhance the visualization of the reaction products. The profiles of sample BB0 presents a distinguishable wide scattering hump at ~26° 2θ. This broad band may be associated to the amorphous structure of metakaolinite. In the figure, the profiles of BB0 and WM0 were kept overlapped to emphasize the shifting in the position of the scattering hump after reaction. The occurrence of a second band at ~33° 2θ was indicative of the partial consumption of metakaolinite to form an X-ray amorphous aluminosilicate phase [69–71], which is referred to as N–A–S–H in low-calcium alkali-activated materials [72].

The peaks of illite and feldspar were preserved, indicating lack of reactivity of these phases in alkaline solution. Low-intensity peaks of thermonatrite and trona, which testify to the carbonation of the alkaline solution, were detected. Thermonatrite exhibited two peaks at ~37° 2θ and just above ~45° 2θ. These peaks were clearly visible in WM0 and scarcely or not detectable within the other blends. WM30, WM40, WM50 showed the presence of trona, with a peak near ~40° 2θ.

Based on the Rietveld quantification on BB0, BB30, BB40, BB50 and on the mix design, the relative fraction of the phases present in the starting mixes were calculated as reported in Table 4. The whole-profile fitting of the XRD patterns relative to the reacted alkali-activated blends did not show significant changes in the relative fraction of calcite, given that the intensity ratios between the main peak of quartz and the main peak of calcite remained approximately constant before and after reaction.

The chemical composition of the matrix of the reacted pastes, as obtained by SEM-EDS microanalysis is summarized in Table 5. The Na/Al atomic ratio varied between 1.3 and 1.8, and the Si/Al ratio between 1.9 and 2.2. This latter ratio is compatible with the stoichiometry of N–A–S–H phases forming in alkali-activated materials [24,34,73]. The presence of excess Na, as compared to typical Na/Al values for N–A–S–H can be associated with the presence of scarcely crystalline sodium carbonate phases (Fig. 11), hardly detectable and quantifiable by XRD investigation. The content of C detected was mainly associated with the graphite coating of the polished sections used for the SEM-EDS analyses and, only secondarily, to CO_2 uptake from the atmosphere. It was observed that the percentage of C increased proportionally to the waste marble content, whereas the percentages of Na, Al, Si decreased. This was indicative of a more porous matrix with less reaction product formed, confirming the microstructural observations.

3.4. Thermodynamic model

The simulated system was simplified by assuming metakaolinite as the sole reactive aluminosilicate source, and excluding inert phases such as quartz, illite and feldspar. The simulations were performed with a progressive increase of CO_2 in the system, with the aim of assessing the effect of carbonation on the phase assemblage. Moreover, it was assumed that the fraction of reacted metakaolinite varied between 25 wt% and 50 wt%, as this would provide a hint of the role of reaction kinetics on the predicted association. More sophisticated
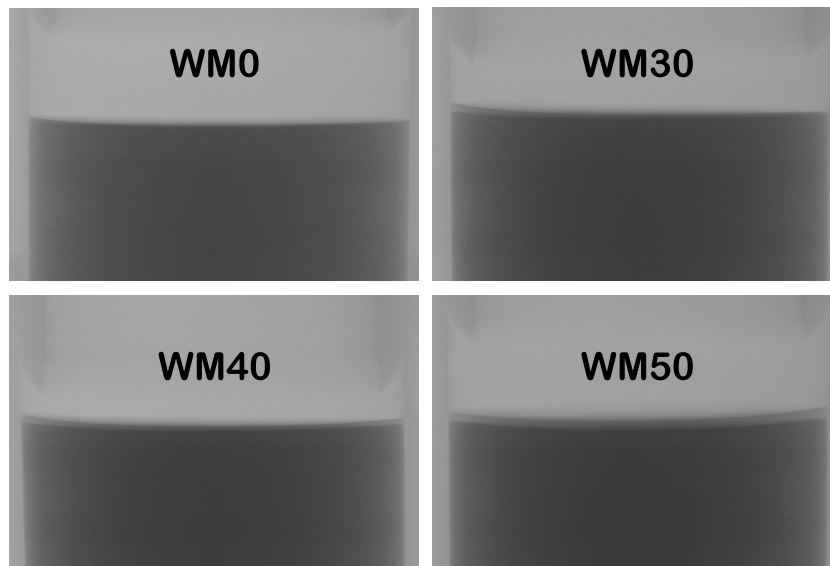
Fig. 6. X-ray attenuation images for the covered samples (bleeding regime) for the alkali-activated samples with different amounts of waste marble, at 3 h since mixing. Light-grey portions of the images, at the sample–air interface, represent bleed layers. The field of view, for each image, is 1.5 cm × 1.0 cm (H × V).
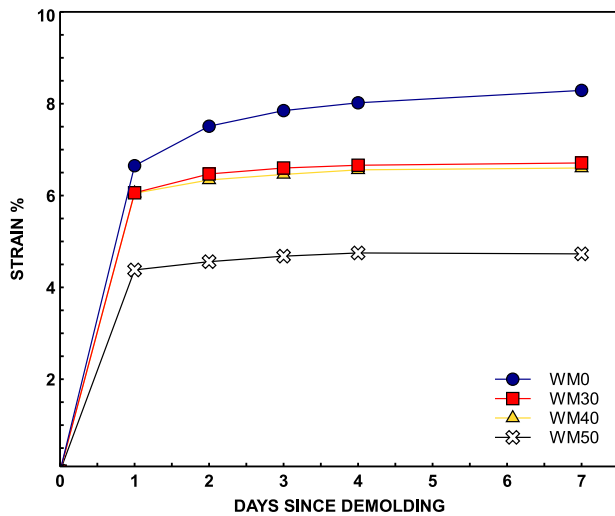

Fig. 7. Vertical strain measured for alkali activated pastes with different amounts of waste marble added. The samples were demoulded after two days of curing at 95% RH and ambient temperature.

Fig. 8. Average compressive strength (bar plot, four measurements per sample) of the alkali-activated pastes. Error bars correspond to standard deviations. White squares represent the values of Na_2O_{eq} for each formulation, normalized to the value of sample WM0.

Table 4

Initial mixes composition (wt.%). All phases were rescaled to the mix design. 1. Calculated by Rietveld phase analysis on the raw clay soil: the relative amount of kaolinite in the raw soil was rescaled to the mass of metakaolinite within the calcined soil (BB0) by considering the mass difference between kaolinite (MM $Al_2Si_2O_5(OH)_4$ = 258.16 g mol^{-1} and 13.96% H_2O) and metakaolinite (MM $Al_2Si_2O_7$ = 222.13 g mol^{-1}). 2. Sum of (partially destructed) illite, feldspar and metaparagonite.

	WM0	WM30	WM40	WM50
Metakaolinite[1]	17.9	13.9	12.3	10.6
Quartz	30.2	23.4	20.7	17.8
Ca-(Mg)-carbonate	0	17.3	23.8	30.8
Other[2]	4.1	3.1	2.8	2.4
Alkaline solution	41.9	32.6	28.8	24.8
Extra water	5.9	9.7	11.6	13.6

Table 5

EDS elemental composition of the matrix of alkali-activated pastes, at 14 days (expressed as mol%, averaged over five matrix points, standard deviation in brackets).

	C	Na	Al	Si	O	Ca
WM0	18.8 (1.4)	6.4 (0.5)	3.9 (0.4)	8.1 (0.8)	62.8 (0.3)	0
WM30	22.0 (0.9)	4.9 (0.6)	2.9 (0.2)	6.2 (0.4)	63.6 (0.3)	0.4 (0.2)
WM40	24.2 (0.7)	4.1 (0.2)	2.2 (0.2)	4.9 (0.3)	64.1 (0.2)	0.6 (0.3)
WM50	25.3 (2.2)	3.1 (0.5)	2.4 (0.9)	4.4 (1.0)	64.7 (0.4)	0.2 (0.1)

models, capable of simulating the reaction kinetics of such systems at reasonably long times, would certainly provide more accurate predictions. Non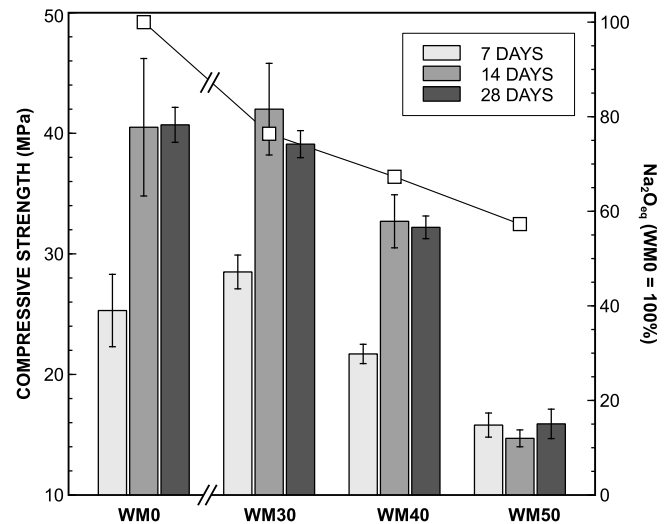etheless, the GEMS thermodynamic model has already proven suitable in providing reliable qualitative predictions on the behaviour of alkali-activated materials [59].

The proportions reported in Table 4 were used to model the reaction product at equilibrium.

The variation of phase association for the four mixes, as a function of the two above parameters, is displayed in Fig. 12 . N–A–S–H was the main reaction product in all samples and its amount decreased proportionally to the amount of waste marble added (hence to the amount of
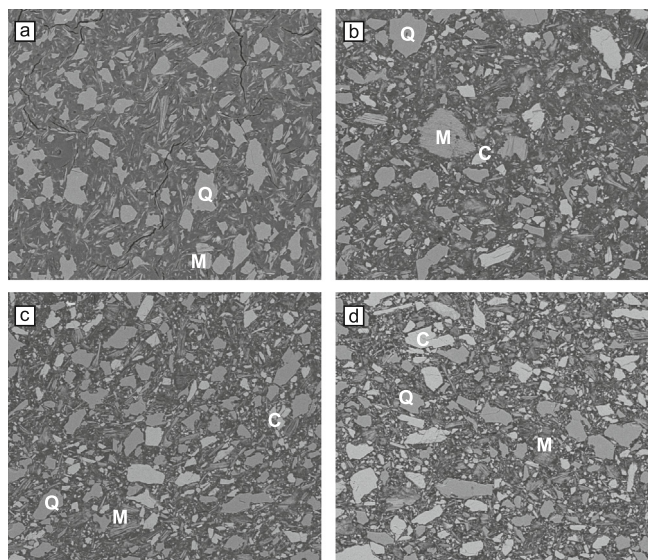
Fig. 9. Backscattered SEM images for samples (prepared at 14 days after mixing) WM0 (a), WM30 (b), WM40 (c), WM50 (d). Labels: M = metakaolinite; Q = quartz; C = calcite. The field of view is 500 μm (H) by 430 μm (V).

metakaolinite substituted). As expected, its amount increased proportionally to the amount of metakaolinite reacted. Also, a slight increase was observed as more CO_2 was drawn into the system.

The model predicted that calcite may dissolve only to a very limited extent, when 25 wt% of metakaolinite reacted. In particular, 1.7 wt% (WM30), 1.1 wt% (WM40) and 0.5 wt% (WM50) were consumed at the lowest CO_2 concentration. Calcium carbonate dissolution progressively reduced to zero as the amount of CO_2 in the system increased. Furthermore, dissolution of calcite was not observed at larger extents of reaction (when 50 wt% of metakaolinite was assumed to be reacted).

Minor amounts of C–(N)–A–S–H were detected in the samples with calcium carbonate additions. It appeared at lower degrees of reaction and at the lowest CO_2 concentration. The amount of C–(N)–A–S–H forming decreased proportionally to the quantity of waste marble.

For the sample with no calcium carbonate addition, the formation of Na carbonates was observed at high CO_2 concentrations. The formation of thermonatrite was first observed, then replacement with trona occurred when CO_2 concentration further increased. For the systems with calcium carbonate additions, thermonatrite was replaced by gaylussite (mixed Na–Ca carbonate) at moderate CO_2 concentrations, whereas at higher concentrations, gaylussite disappeared and trona formed, in sample WM30 only. Precipitation of pirssonite, the other Na–Ca carbonate included in the database, was never observed. Overall, at high levels of CO_2 uptake, the total amount of carbonates decreased proportionally to the quantity of waste marble added.

In general, alkaline carbonates and C–(N)–A–S–H appeared to be metastable, and tended to decrease in concentration or disappear as more metakaolinite reacted with the alkaline solution.

4. Discussion

The effect of calcium carbonate additions to high purity metakaolin was elegantly discussed in a series of recent papers [23–25]. Here, we intentionally chose a low-grade clay (having less than 50 wt% kaolinite) to assess the feasibility of (waste) calcium carbonate additions to an aluminosilicate source. In fact, local clayey formations may represent a more economically advantageous raw material compared to nearly pure metakaolin.

From the point of view of fresh properties, it was observed that the addition of waste marble allowed pastes with the same workability to be produced with reduced amounts of aqueous solution,

proportionally to the level of clay substitution. This effect was expected, given the tendency of phyllosilicate minerals to absorb water, especially when they are subject to calcination at relatively high temperatures [74]. For example, a previous study showed that increasing the limestone/calcined-clay ratio in ternary cement blends enhances paste workability [75].

The viscosity curves displayed in Fig. 3 showed that, even by formulating the mixes incorporating waste marble with reduced amounts of aqueous solutions, at relatively high shear rates the viscosity decreased as the amount of waste marble increased, which was indicative of enhanced paste mixing. At low shear, it was observed that viscosity increased proportionally to the amount of waste marble present in the mix. Intuitively, it could be envisaged that, as a consequence, pastes with higher amounts of waste marble would undergo less particle settling while being in the fresh state, given that, according to Stokes' law, settling velocity decreases with increasing viscosity. On the contrary, the early-age shrinkage measurements performed in the bleeding regime demonstrated a significantly stronger tendency to settling and bleeding for the sample with the highest amount of waste marble (Figs. 5 and 6). This behaviour can be explained by means of the theory of the scaling behaviour of the elastic properties of colloidal gels [76]. A recent study carried out on calcite suspension demonstrated, based on this theory, that by increasing the concentration of calcite, a transition occurs from a system dominated by inter-particle links, to one consisting of interconnected dense flocs [77]. A similar transition was envisaged for the mixes investigated in the present study, where increasing the amount of waste marble from 40 wt% to 50 wt% might have led to the formation of denser calcite flocs that exhibited enhanced elastic properties (as evidenced by the larger G' to G'' ratio, Fig. 4) and a stronger tendency to settle. When shear is increased, rupture of the links between these flocs leads to a significant decrease in viscosity (Fig. 3). An adequate curing schedule might reduce the large shrinkage occurring in the hardened state, which may be a point of concern. The results showed that most of the measured shrinkage occurred during the first day after removal of the samples from the high RH environment. Specific curing strategies and the use of shrinkage reducing admixtures may help mitigating this issue [78–80]. However, for the purpose of the present study, it was observed that the addition of waste marble positively affects dimensional stability in the hardened state, by reducing the strain measured at one week by 25 to 50%. This effect was likely due to the reduced amount of aqueous solution needed in the presence of waste marble additions. Previous studies suggested that the measured shrinkage of alkali-activated cements increased proportionally to the amount of sodium silicate activator used [67].

In terms of mechanical properties, the results presented here were in line with those of previous studies showing that moderate additions of calcium carbonate did not significantly affect, or even improve the compressive strength of alkali-activated calcined clays [19,20,22,23]. In this study, the mechanical properties were negatively affected for additions larger than 30 wt%, compared to maximum levels of substitutions of about 60 wt% suggested in the cited studies. However, it has to be taken into account that the clay soil used here contained a large fraction of inert phases such as quartz. Therefore, in the present case, 30 wt% substitution corresponded to a mix design with nearly equal amounts, by mass, of metakaolinite and calcium carbonate (Table 4).

Some authors argued that the improvement of mechanical properties, in the presence of calcium carbonate additions, were solely related to an enhanced particle packing with calcite crystals acting as inert fillers [21,22]. Others suggested that a limited calcite dissolution contributed to the formation of C–(N)–A–S–H phase that may positively affect the mechanical performance [19,20,24]. In our study, the results of XRD analysis did not suggest significant calcite dissolution after 14 days of reaction. Thermodynamic modelling predicted calcite to dissolve in quantities lower than 2 wt%, only at relatively low degree
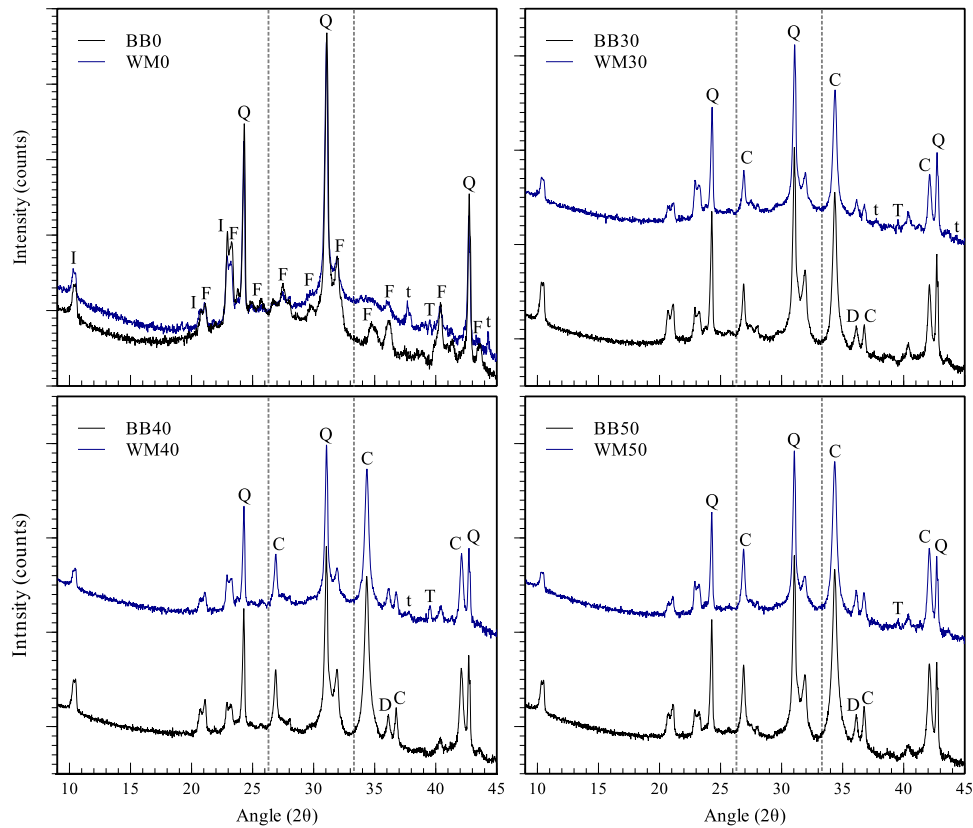
Fig. 10. XRD diffraction patterns of the unreacted (BB0, BB30, BB40, BB50) and reacted mixes (WM0, WM30, WM40, WM50) at 14 days. Phase labels: I = illite; F = feldspar; t = thermonatrite; *T* = trona; Q = quartz; C = calcite; D = dolomite. The grey dotted lines emphasize the expected position of the centre of the scattering hump before and after reaction. The first at ~26° 2θ was associated to metakaolinite, the second at ~33° 2θ was associated to N–A–S–H.
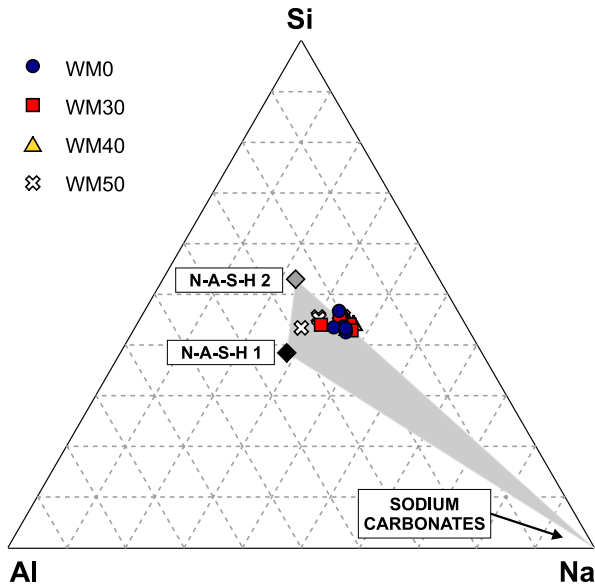

Fig. 11. Si–Al–Na triangular plot (mol%) displaying the chemical composition of the matrix of the reacted pastes, as obtained by EDS microanalysis. Diamonds correspond to the composition of synthetic N–A–S–H end-members [52], which are used for the thermodynamic model in this study. The grey area represents the set of theoretical compositions of finely dispersed mixture of N–A–S–H and sodium carbonates.

at the early stages of reaction. Afterwards, uptake of atmospheric CO_2 may possibly induce re-precipitation of calcite. Therefore, dissolution of calcite grains occurred only to a limited extent, but was not negligible as also testified by the presence of Ca in the matrix of the hardened material. To link the system chemical and mineralogical evolution to the macroscopic observations, we attempted to semi-quantitatively estimate the matrix composition based on the microchemical analysis obtained by SEM-EDS. These calculations were carried out based on the assumptions that: (1) all Si and Al present in the matrix were incorporated in a N–A–S–H reaction product having the stoichiometry of N–A–S–H 1, which was the dominant end-member predicted by thermodynamic modelling; (2) the amount of C–(N)–A–S–H was negligible, based on the results of the thermodynamic modelling, showing that if any C–(N)–A–S–H formed, it was highly metastable and subjected to carbonation (Fig. 12); (3) the excess fraction of Na, not incorporated in N–A–S–H was partitioned in alkaline carbonates, with thermonatrite being the dominant Na-carbonate in WM0, and trona in blends with waste marble additions, as observed by XRD; (4) Ca present in the matrix was attributed to gaylussite, which was predicted by thermodynamic modelling; (5) C (from the sample thin graphite coating applied before the SEM analysis) preferentially filled pores, and was used as a proxy of the matrix porosity.

The results of these calculations were summarized in Fig. 13. Based on the elemental composition, part of the N–A–S–H reaction product was replaced by alkali carbonates, due to CO_2 uptake from the atmosphere. The EDS-recalculated phase association indicated a progressively smaller amount of trona proportionally to the amount of waste marble present in the system. Small quantities of trona were also detected by XRD analysis that, on the contrary, was not capable of detecting gaylussite. This might be related to the possible presence of poorly crystalline carbonates. The formation of amorphous carbonates during cement carbonation, as precursors of crystalline phases, was
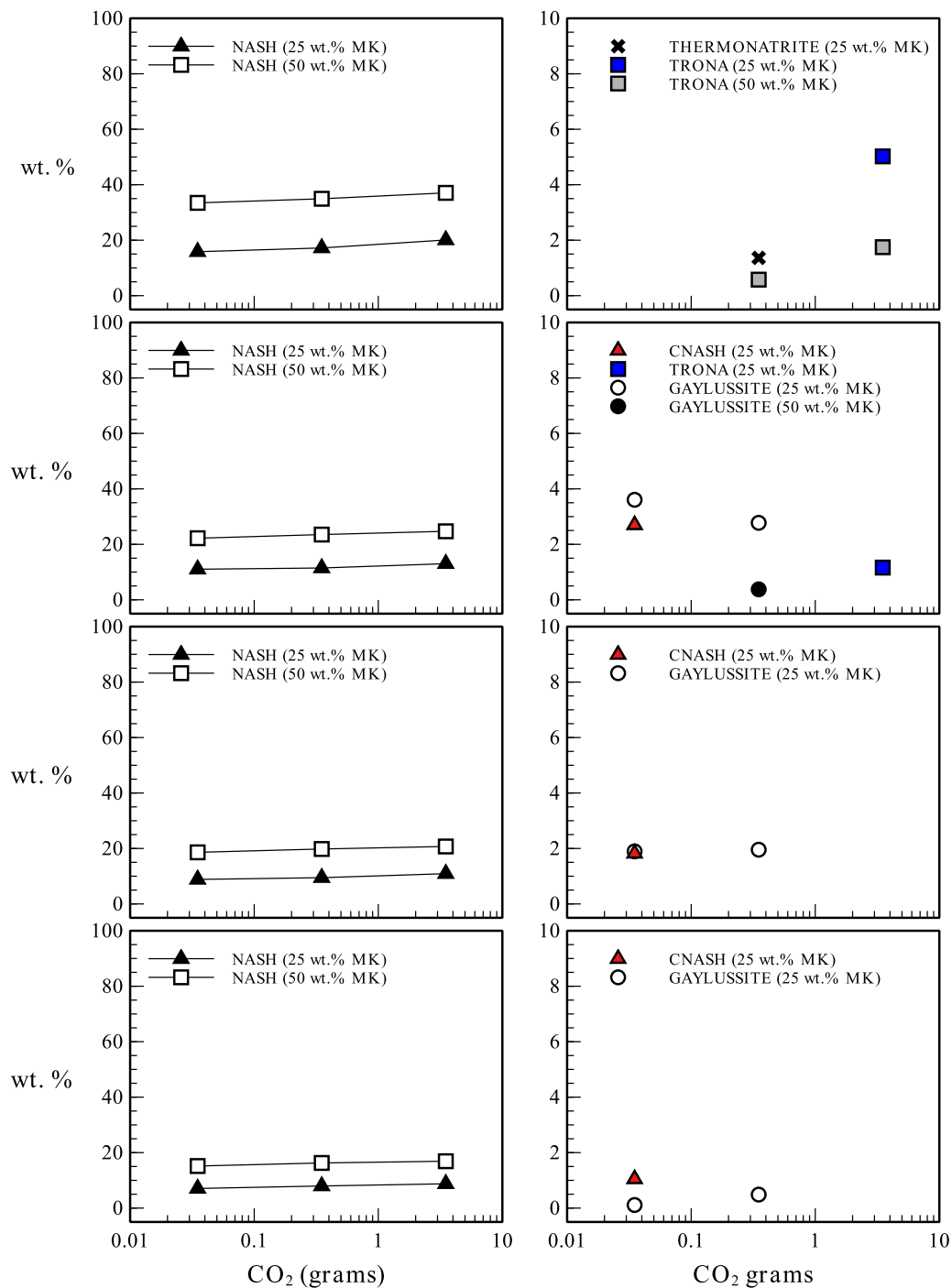
of reaction (25 wt% metakaolinite dissolution) and low CO_2 concentrations. Therefore, we argue that only limited amounts of calcium carbonate may take part in the reaction with sodium silicate solution

Fig. 12. Simulated composition of the reaction product for samples (top to bottom) WM0, WM30, WM40, WM50, at 25 wt% and 50 wt% metakaolinite consumption, and for different levels of system carbonation. The graphs on the left display the amount of N–A–S–H formed. The graphs on the right display phases precipitating in minor amounts.

observed in previous studies [81,82]. The thermodynamic model also predicted that gaylussite was consumed as more metakaolinite reacted. Since gaylussite incorporates a higher amount of water compared to trona, its consumption and dehydration, leading to the formation of calcite and trona, might result in extra porosity, according to the reaction:

$$3Na_2Ca(CO_3)_2 \cdot 5H_2O + CO_2$$
$$\longrightarrow 3CaCO_3 + 2Na_3(CO_3)(HCO_3) \cdot 2(H_2O) + 10H_2O \qquad (1)$$
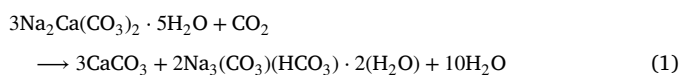
This reaction could have detrimental effects on the matrix [83], which in turn might possibly explain the observed slight reduction in compressive strength from 14 to 28 days for samples WM30 and WM40.

5. Conclusions

Previous studies showed that the addition of limestone to alkali-activated cements with high amounts of metakaolinite may improve some properties of the binder as well as the overall environmental performance. Here, we showed that this approach can be replicated
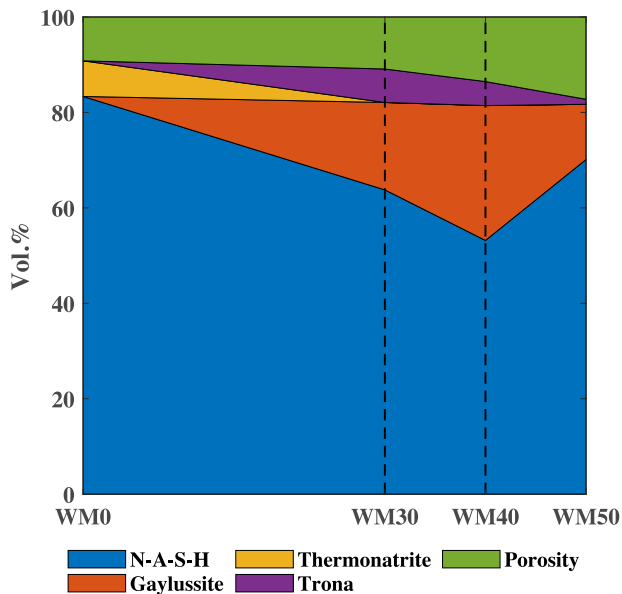
Fig. 13. Matrix phase composition estimated from the SEM-EDS phase analysis, expressed as volume percentage (Vol.%) of the total matrix.

on raw materials consisting of low-grade clay soils, comprising less than 50 wt% kaolinite. Furthermore, primarily sourced limestone was replaced with a secondary raw material deriving from the marble industry.

With respect to mechanical properties, we observed that compressive strength in the presence of 30 wt% waste marble was comparable to the one measured in the absence of calcium carbonate addition. The fact that, based on our result, only limited amounts of calcium carbonate seem to take part in the reaction, suggest that the diminished amount of reactive aluminosilicate is compensated by a microstructural effect of the calcite crystals present in waste marble, which may enhance particle packing, acting as micro-aggregates. Moreover, at 30 wt% level of calcined clay substitution with waste marble, a reduction of 25% Na_2O_{eq} is achieved, indicating a potential significant reduction in CO_2 emissions embodied in the alkaline activator. Although compressive strength was observed to the decrease at 40 wt% level substitution of calcined clay with waste marble, the 28 days compressive strength was still higher than 30 MPa, with a reduction in Na_2O_{eq} of more than 30 wt%.

In summary, potential benefits in terms of overall environmental impact derived from: (a) reduced amount of alkaline activator, with its embodied CO_2 needed in the formulation; (b) lower volume of material requiring thermal treatment; (c) valorization of dimension stone waste streams (marble slurry). Regarding point (c), we encourage further investigation of this approach using waste from the stone industry other than marble slurry, e.g. granite and dolomite waste, depending on local availability.

To conclude, the results of this study on alkali-activated calcined clay demonstrated that the use of moderate amounts of waste marble (30%) in place of calcined clay soil: (a) improves or does not negatively affect compressive strength; (b) improves paste workability; (c) mitigates drying shrinkage. Plastic and early-age shrinkage, on the other hand, increased proportionally to the amount of waste marble added, but the difference with formulations without any additions can be minimized by adopting a curing regime that prevents evaporation.

In terms of microscopic properties, by combining the results from XRD, SEM-EDS microchemical analysis and thermodynamic modelling, it was demonstrated that the reaction product mainly consists of N–A–S–H with minor amounts of alkaline carbonates deriving from the

reaction of the alkaline solution with atmospheric CO_2. Calcite crystals within waste marble mostly acted as filler, with a very limited extent of dissolution. This small amount of Ca ions released in solution may form minor quantities of C–(N)–A–S–H that, based on the results of thermodynamic modelling, tended to be destabilized in favour of gaylussite. Gaylussite itself may represent a metastable phase and converted to trona and calcite as more metakaolinite reacted and further atmospheric CO_2 was drawn into the system. Specific investigations aimed at clarifying the role of carbonation, and verifying the theoretical predictions obtained by thermodynamic modelling, would certainly contribute to a better understanding of the chemical pathways that control the reactivity of such alkali-activated blends and their role in determining the macroscopic properties of these materials.

Declaration of competing interest

The authors declare that they have no known competing financial interests or personal relationships that could have appeared to influence the work reported in this paper.

References

[1] Circle Economy, Circularity Gap Report 2021, Tech. rep., 2021.
[2] UNEP, Eco-Efficient Cements: Potential Economically Viable Solutions for a Low-CO_2 Cement-Based Materials Industry, United Nations Environment Programme, Geneva, Switzerland, 2017.
[3] UNEP, Sand and Sustainability: Finding New Solutions for Environmental Governance of Global Sand Resources, United Nations Environment Programme, Geneva, Switzerland, 2019.
[4] C.N. Waters, J. Zalasiewicz, C. Summerhayes, A.D. Barnosky, C. Poirier, A. Gałuszka, A. Cearreta, M. Edgeworth, E.C. Ellis, M. Ellis, C. Jeandel, R. Leinfelder, J.R. McNeill, D.d. Richter, W. Steffen, J. Syvitski, D. Vidas, M. Wagreich, M. Williams, A. Zhisheng, J. Grinevald, E. Odada, N. Oreskes, A.P. Wolfe, The anthropocene is functionally and stratigraphically distinct from the holocene, Science 351 (6269) (2016).
[5] C. Montani, XXVIII World Marble and Stones Report, Tech. rep., 2017.
[6] G. Rizzo, F. D'Agostino, L. Ercoli, Problems of soil and groundwater pollution in the disposal of "marble" slurries in NW Sicily, Environ. Geol. 55 (2008) 929–935.
[7] N. Careddu, G. Siotto, Promoting ecological sustainable planning for natural stone quarrying. the case of the Orosei Marble Producing Area in Eastern Sardinia, Resour. Policy 36 (4) (2011) 304–314.
[8] S. Mulk, A. Azizullah, A. Korai, M. Khattak, Impact of marble industry effluents on water and sediment quality of Barandu River in Buner District, Pakistan, Environ. Monit. Assess. 187 (2015) 8.
[9] H.Y. Aruntas, M. Guru, M. Dayi, I. Tekin, Utilization of waste marble dust as an additive in cement production, Mater. Des. 31 (8) (2010) 4039–4042.
[10] A. Belaidi, L. Azzouz, E. Kadri, S. Kenai, Effect of natural pozzolana and marble powder on the properties of self-compacting concrete, Constr. Build. Mater. 31 (2012) 251–257.
[11] A. Rana, P. Kalla, L.J. Csetenyi, Sustainable use of marble slurry in concrete, J. Cleaner Prod. 94 (2015) 304–311.
[12] A.O. Mashaly, B.A. El-Kaliouby, B.N. Shalaby, A.M. El – Gohary, M.A. Rashwan, Effects of marble sludge incorporation on the properties of cement composites and concrete paving blocks, J. Cleaner Prod. 112 (2016) 731–741.
[13] S. Krishnan, S.K. Kanaujia, S. Mithia, S. Bishnoi, Hydration kinetics and mechanisms of carbonates from stone wastes in ternary blends with calcined clay, Constr. Build. Mater. 164 (2018) 265–274.
[14] L. Ricciotti, A. Molino, V. Roviello, E. Chianese, P. Cennamo, G. Roviello, Geopolymer composites for potential applications in cultural heritage, Environments 4 (2017) 91.
[15] L. Valentini, S. Contessi, M.C. Dalconi, F. Zorzi, E. Garbin, Alkali-activated calcined smectite clay blended with waste calcium carbonate as a low-carbon binder, J. Cleaner Prod. 184 (2018) 41–49.
[16] B. Coppola, P. Palmero, L. Montanaro, J.-M. Tulliani, Alkali-activation of marble sludge: Influence of curing conditions and waste glass addition, J. Eur. Ceram. Soc. (2019).
[17] E. El-Alfi, R. Gado, Preparation of calcium sulfoaluminate-belite cement from marble sludge waste, Constr. Build. Mater. 113 (2016) 764–772.
[18] J.L. Provis, Alkali-activated materials, Cem. Concr. Res. 114 (2018) 40–48.
[19] C.K. Yip, J.L. Provis, G.C. Lukey, J.S. van Deventer, Carbonate mineral addition to metakaolin-based geopolymers, Cem. Concr. Compos. 30 (10) (2008) 979–985.
[20] A. Cwirzen, J.L. Provis, V. Penttala, K. Habermehl-Cwirzen, The effect of limestone on sodium hydroxide-activated metakaolin-based geopolymers, Constr. Build. Mater. 66 (2014) 53–62.

[21] A. Aboulayt, M. Riahi, M.O. Touhami, H. Hannache, M. Gomina, R. Moussa, Properties of metakaolin based geopolymer incorporating calcium carbonate, Adv. Powder Technol. 28 (9) (2017) 2393–2401.

[22] B.N. Bayiha, N. Billong, E. Yamb, R.C. Kaze, R. Nzengwa, Effect of limestone dosages on some properties of geopolymer from thermally activated halloysite, Constr. Build. Mater. 217 (2019) 28–35.

[23] P. Perez-Cortes, J.I. Escalante-Garcia, Alkali activated metakaolin with high limestone contents – Statistical modeling of strength and environmental and cost analyses, Cem. Concr. Compos. 106 (2020) 103450.

[24] P. Perez-Cortes, J.I. Escalante-Garcia, Gel composition and molecular structure of alkali-activated metakaolin-limestone cements, Cem. Concr. Res. 137 (2020) 106211.

[25] P. Perez-Cortes, J.I. Escalante-Garcia, Design and optimization of alkaline binders of limestone-metakaolin – A comparison of strength, microstructure and sustainability with portland cement and geopolymers, J. Cleaner Prod. 273 (2020) 123118.

[26] K.-H. Yang, J.-K. Song, K.-I. Song, Assessment of CO_2 reduction of alkali-activated concrete, J. Cleaner Prod. 39 (2013) 265–272.

[27] G. Habert, C. Ouellet-Plamondon, Recent update on the environmental impact of geopolymers, RILEM Tech. Lett. 1 (2016).

[28] G. Dino, C. Chiappino, P. Rossettii, Quarry waste management and recovery: first results connected to Carrara marble Ravaneti (Italy), in: Geophysical Research Abstracts, EGU - European Geosciences Union, 2017.

[29] EN 933-1: 2012, Tests for geometrical properties of aggregates. Determination of particle size distribution. Sieving method, 2012.

[30] N. Doebelin, R. Kleeberg, *Profex*: a graphical user interface for the rietveld refinement program *bgmn*, J. Appl. Crystallogr. 48 (5) (2015) 1573–1580.

[31] L. Mascarin, Characterization and thermodynamic modelling of alkali-activated calcined clays: potentiality of Cameroon's laterites as eco-sustainable binders (Master's thesis), University of Padua, 2018.

[32] C. Chen, G. Lan, W. Tuan, Microstructural evolution of mullite during the sintering of kaolin powder compacts, Ceram. Int. 26 (7) (2000) 715–720.

[33] A. Shvarzman, K. Kovler, G. Grader, G. Shter, The effect of dehydroxylation/amorphization degree on pozzolanic activity of kaolinite, Cem. Concr. Res. 33 (3) (2003) 405–416.

[34] R. Fernandez, F. Martirena, K.L. Scrivener, The origin of the pozzolanic activity of calcined clay minerals: A comparison between kaolinite, illite and montmorillonite, Cem. Concr. Res. 41 (1) (2011) 113–122.

[35] P. Ptáček, F. Frajkorová, F. Šoukal, T. Opravil, Kinetics and mechanism of three stages of thermal transformation of kaolinite to metakaolinite, Powder Technol. 264 (2014) 439–445.

[36] J.P. Schelz, The detection of quartz in clay minerals by differential thermal analysis, Thermochim. Acta 15 (1) (1976) 17–28.

[37] P. Comodi, P. Zanazzi, Structural thermal behavior of paragonite and its dehydroxylate: a high-temperature single-crystal study, Phys. Chem. Miner. 27 (6) (2000) 377–385.

[38] J. Schomburg, H. Zwahr, Thermal differential diagnosis of mica mineral group, J. Therm. Anal. 48 (1) (1997) 135–139.

[39] M. El Ouahabi, L. Daoudi, F. Hatert, N. Fagel, Modified mineral phases during clay ceramic firing, Clays Clay Miner. 63 (2015) 404–413.

[40] H. Wang, C. Li, Z. Peng, S. Zhang, Characterization and thermal behavior of kaolin, J. Therm. Anal. Calorim. 105 (1) (2011) 157–160.

[41] L. Valentini, AMiDsT v1.0 Alkali-activated-materials Mix Design Tool. Documentation, http://dx.doi.org/10.13140/RG.2.2.18905.47200/1.

[42] T. Luukkonen, Z. Abdollahnejad, J. Yliniemi, P. Kinnunen, M. Illikainen, One-part alkali-activated materials: A review, Cem. Concr. Res. 103 (2018) 21–34.

[43] L. Valentini, L. Mascarin, Assessing the dimensional stability of alkali-activated calcined clays in the fresh state: a time-lapse X-ray imaging approach, Mater. Struct. 54 (2021) 35.

[44] F. Jin, K. Gu, A. Al-Tabbaa, Strength and drying shrinkage of reactive MgO modified alkali-activated slag paste, Constr. Build. Mater. 51 (2014) 395–404.

[45] M. Hojati, F. Rajabipour, A. Radlińska, Drying shrinkage of alkali-activated cements: effect of humidity and curing temperature, Mater. Struct. 52 (6) (2019) 118.

[46] X. Hu, C. Shi, Z. Zhang, Z. Hu, Autogenous and drying shrinkage of alkali-activated slag mortars, J. Am. Ceram. Soc. 102 (8) (2019) 4963–4975.

[47] EN 196-1: 2016, Methods of testing cement, in: Determination of strength, 2016.

[48] J. Zhang, G.W. Scherer, Comparison of methods for arresting hydration of cement, Cem. Concr. Res. 41 (10) (2011) 1024–1036.

[49] X. Chen, A. Meawad, L.J. Struble, Method to stop geopolymer reaction, J. Am. Ceram. Soc. 97 (10) (2014) 3270–3275.

[50] D.A. Kulik, T. Wagner, S.V. Dmytrieva, G. Kosakowski, F.F. Hingerl, K.V. Chudnenko, U.R. Berner, GEM-selektor geochemical modeling package: revised algorithm and GEMS3K numerical kernel for coupled simulation codes, Comput. Geosci. 17 (1) (2013) 1–24.

[51] L. Valentini, Modeling dissolution–precipitation kinetics of alkali-activated metakaolin, ACS Omega 3 (12) (2018) 18100–18108.

[52] L. Gomez-Zamorano, M. Balonis, B. Erdemli, N. Neithalath, G. Sant, C–(N)–S–H and N–A–S–H Gels: Compositions and solubility data at 25 °C and 50 °C, J. Am. Ceram. Soc. 100 (6) (2017) 2700–2711.

[53] L. Qiu, V. Murashov, M.A. White, Zeolite 4A: heat capacity and thermodynamic properties, Solid State Sci. 2 (8) (2000) 841–846.

[54] B. Zhen-Wu, D. Prentice, J. Ryan, K. Ellison, M. Bauchy, G. Sant, Zeo19: A thermodynamic database for assessing zeolite stability during the corrosion of nuclear waste immobilization glasses, Npj Mater. Degrad. 4 (2) (2020).

[55] R.J. Myers, S.A. Bernal, J.L. Provis, A thermodynamic model for C–(N–)A–S–H gel: Cnash_ss. Derivation and validation, Cem. Concr. Res. 66 (2014) 27–47.

[56] S.A. Bernal, J.L. Provis, D.G. Brice, A. Kilcullen, P. Duxson, J.S. van Deventer, Accelerated carbonation testing of alkali-activated binders significantly underestimates service life: The role of pore solution chemistry, Cem. Concr. Res. 42 (10) (2012) 1317–1326.

[57] B. Dickens, W.E. Brown, Crystal structures of $CaNa_2(CO_3) \cdot 2.5H_2O$, synthetic gaylussite, and $CaNa_2(CO_3) \cdot 2.2H_2O$, synthetic pirssonite, Inorg. Chem. 8 (10) (1969) 2093–2103.

[58] T. Thoenen, W. Hummel, U. Berner, E. Curti, The PSI/Nagra Chemical Thermodynamic Database 12/07, Tech. rep., Paul Scherrer Institut, 2014.

[59] X. Ke, S.A. Bernal, J.L. Provis, B. Lothenbach, Thermodynamic modelling of phase evolution in alkali-activated slag cements exposed to carbon dioxide, Cem. Concr. Res. 136 (2020) 106158.

[60] N. Schieltz, N. Soliman, Thermodynamics of the various high temperature transformations of kaolinite, in: Proceedings of the 13th National Conference on Clays and Clay Minerals, Pergamon Press, NY, 1966, pp. 419–428.

[61] K. Vance, A. Arora, G. Sant, N. Neithalath, Rheological evaluations of interground and blended cement–limestone suspensions, Constr. Build. Mater. 79 (2015) 65–72.

[62] S. Ghourchian, M. Wyrzykowski, P. Lura, A poromechanics model for plastic shrinkage of fresh cementitious materials, Cem. Concr. Res. 109 (2018) 120–132.

[63] H. Ez-zaki, J.M. Marangu, M. Bellotto, M. Dalconi, G. Artioli, L. Valentini, A fresh view on limestone calcined clay cement (LC^3) pastes, Materials 14 (11) (2021) 3037.

[64] T. Cheng, J. Chiu, Fire-resistant geopolymer produced by granulated blast furnace slag, Miner. Eng. 16 (3) (2003) 205–210.

[65] P.D. Silva, K. Sagoe-Crenstil, V. Sirivivatnanon, Kinetics of geopolymerization: Role of Al_2O_3 and SiO_2, Cem. Concr. Res. 37 (4) (2007) 512–518.

[66] S.A. Bernal, J.L. Provis, V. Rose, R. Mejía de Gutierrez, Evolution of binder structure in sodium silicate-activated slag-metakaolin blends, Cem. Concr. Compos. 33 (1) (2011) 46–54.

[67] A.A. Melo Neto, M.A. Cincotto, W. Repette, Drying and autogenous shrinkage of pastes and mortars with activated slag cement, Cem. Concr. Res. 38 (4) (2008) 565–574.

[68] J.L. Provis, K. Arbi, S.A. Bernal, D. Bondar, A. Buchwald, A. Castel, S. Chithiraputhiran, M. Cyr, A. Dehghan, K. Dombrowski-Daube, A. Dubey, V. Ducman, G.J.G. Gluth, S. Nanukuttan, K. Peterson, F. Puertas, A. van Riessen, M. Torres-Carrasco, G. Ye, Y. Zuo, RILEM TC 247-DTA round robin test: mix design and reproducibility of compressive strength of alkali-activated concretes, Mater. Struct. 52 (5) (2019) 99.

[69] J.L. Provis, G.C. Lukey, J.S.J. van Deventer, Do geopolymers actually contain nanocrystalline zeolites? A reexamination of existing results, Chem. Mater. 17 (12) (2005) 3075–3085.

[70] R.P. Williams, R.D. Hart, A. van Riessen, Quantification of the extent of reaction of metakaolin-based geopolymers using X-Ray diffraction, scanning electron microscopy, and energy-dispersive spectroscopy, J. Am. Ceram. Soc. 94 (8) (2011) 2663–2670.

[71] Z. Sun, A. Vollpracht, Isothermal calorimetry and in-situ XRD study of the NaOH activated fly ash, metakaolin and slag, Cem. Concr. Res. 103 (2018) 110–122.

[72] J.L. Provis, S.A. Bernal, Geopolymers and related alkali-activated materials, Annu. Rev. Mater. Res. 44 (2014) 299–327.

[73] I. Garcia-Lodeiro, A. Palomo, A. Fernández-Jiménez, D. Macphee, Compatibility studies between N–A–S–H and C–A–S–H gels. Study in the ternary diagram Na_2O–CaO–Al_2O_3–SiO_2–H_2O, Cem. Concr. Res. 41 (9) (2011) 923–931.

[74] A. Neißer-Deiters, S. Scherb, N. Beuntner, K.-C. Thienel, Influence of the calcination temperature on the properties of a mica mineral as a suitability study for the use as SCM, Appl. Clay Sci. 179 (2019) 105168.

[75] T.R. Muzenda, P. Hou, S. Kawashima, T. Sui, X. Cheng, The role of limestone and calcined clay on the rheological properties of LC^3, Cem. Concr. Compos. 107 (2020) 103516.

[76] W.-H. Shih, W.Y. Shih, S.-I. Kim, S. Liu, I.A. Aksay, Scaling behavior of the elastic properties of colloidal gels, Phys. Rev. A 42 (1990) 4772–4779.

[77] T. Liberto, M. Le Merrer, C. Barentin, M. Bellotto, J. Colombani, Elasticity and yielding of a calcite paste: scaling laws in a dense colloidal suspension, Soft Matter 13 (2017) 2014–2023.

[78] M. Palacios, F. Puertas, Effect of shrinkage-reducing admixtures on the properties of alkali-activated slag mortars and pastes, Cem. Concr. Res. 37 (5) (2007) 691–702.

[79] R. Thomas, D. Lezama, S. Peethamparan, On drying shrinkage in alkali-activated concrete: Improving dimensional stability by aging or heat-curing, Cem. Concr. Res. 91 (2017) 13–23.

[80] M. Češnovar, K. Traven, V. Ducman, Deformation of alkali-activated materials at an early age under different curing conditions, Front. Chem. 9 (2021) 378.

[81] Ö. Cizer, C. Rodriguez-Navarro, E. Ruiz-Agudo, J. Elsen, D. Van Gemert, K. Van Balen, Phase and morphology evolution of calcium carbonate precipitated by carbonation of hydrated lime, J. Mater. Sci. 47 (16) (2012) 6151–6165.

[82] Ö. Cizer, K. Van Balen, J. Elsen, D. Van Gemert, Real-time investigation of reaction rate and mineral phase modifications of lime carbonation, Construc. Build. Mater. 35 (2012) 741–751.

[83] B. Yuan, Q. Yu, H. Brouwers, Phase modification induced drying shrinkage reduction on Na_2CO_3 activated slag by incorporating Na_2SO_4, Mater. Struct. 50 (2017) 220.